crystals

MDPI

Article

The Influence of Silica Template Aging Temperature on the Properties and Catalytic Activity of Nanocast Mesoporous Zirconium-Doped Ceria

Katarina Mužina [1], Jakov-Stjepan Pavelić [2], Filip Car [1], Filip Brleković [1], Goran Dražić [2], Lara Mikac [3], Gordana Matijašić [1], Vesna Tomašić [1] and Stanislav Kurajica [1,*]

[1] Faculty of Chemical Engineering and Technology, University of Zagreb, HR-10000 Zagreb, Croatia; kmuzina@fkit.unizg.hr (K.M.); fcar@fkit.unizg.hr (F.C.); fbrlekovi@fkit.unizg.hr (F.B.); gmatijas@fkit.unizg.hr (G.M.); vtomas@fkit.unizg.hr (V.T.)
[2] National Institute of Chemistry, 1000 Ljubljana, Slovenia; jakov-stjepan.pavelic@ki.si (J.-S.P.); goran.drazic@gmail.com (G.D.)
[3] Ruđer Bošković Institute, HR-10000 Zagreb, Croatia; lmikac@irb.hr
[*] Correspondence: stankok@fkit.unizg.hr

Abstract

KIT-6 samples were prepared at hydrothermal aging temperatures of 60, 100, and 140 °C, and used as templates for nanocasting of zirconium-doped ceria. In nanocast samples, the ordered 3D structure collapsed, leaving behind nanorods with a diameter roughly in concordance with the corresponding KIT-6 template pore diameter. In addition to nanocrystalline ceria, a small amount of cubic zirconia is present in the doped samples, but the formation of a solid solution was confirmed by the decrease in the ceria lattice parameter relative to bulk ceria. The specific surface areas of the nanocast samples decreased with the increase in KIT-6 template aging temperature. Ceria bandgap values were slightly blueshifted in comparison with bulk ceria, which was attributed to quantum confinement. No difference between samples concerning lattice ceria defects has been noted. Conversion curves show apparent three-stage conversion with stagnation at temperatures in the range between 250 °C and 300 °C, which is a consequence of abundant adsorption of toluene below 250 °C and desorption above 250 °C. Slight differences in catalytic activity are only due to a difference in the amount of adsorbed toluene caused by differences in the specific surface area of the samples.

Keywords: nanocasting; zirconium doped ceria; mesostructured; nanorods; three-stage conversion

Check for updates

Academic Editor: Raluca Mereu

Received: 11 December 2025
Revised: 20 January 2026
Accepted: 21 January 2026
Published: 24 January 2026

1. Introduction

Mesoporous materials have proven useful in various fields such as renewable energy storage and conversion [1,2], imaging and drug delivery [3,4], catalysis [5,6], etc. Silica-based mesoporous materials are most frequently used due to their ability to form various mesostructures with tunable pore sizes and large surface areas [7,8]. In addition to being used for various functional applications, due to their ordered mesoporous structure, mesostructured silica-based materials have also been utilized as nanocasting templates. Various mesostructured silica materials, such as the two-dimensional SBA-15 and the three-dimensional KIT-6, were employed as templates for nanocasting of different oxides [9,10]. KIT-6 turned out to be particularly suitable as a hard template due to its bicontinuous

https://doi.org/10.3390/cryst16020083

three-dimensional microstructure with interpenetrating cylindrical pores having large diameters [11], which could be easily tuned by changing the synthesis conditions [12].

The synthesis of mesostructured silica materials is based on the use of structure-directing agents such as triblock copolymer Pluronic 123. Under appropriate conditions, the structure-directing agent self-assembles into micelles, which act as a template for silica deposition. In the course of the sol-gel process, a silica precursor such as TEOS (Tetraethyl Orthosilicate) is added, and the formed silica is deposited around the micelles whose architecture directs the formation of mesostructured silica. Once the silica is formed, the template is removed, and the remaining material has the structure of ordered mesopores, being the negative replica of the original micelle architecture [13]. The mesoporous structure of mesostructured silica materials, as well as key properties such as pore size, pore size distribution, pore connectivity, wall thickness, and specific surface area (SSA), can be controlled by using structure-directing agents and by adjusting synthesis conditions such as reaction time or temperature [11]. For example, by changing the hydrothermal aging temperature, the pore size of KIT-6 can be tuned from 4 to 12 nm [12]. The properties of the template later play a decisive role in determining the properties of the nanocast material, especially textural and microstructural properties.

Ceria (CeO_2) and ceria-based systems are widely applied as catalysts and catalyst supports in a wide range of processes [14–17]. Ceria is characterized by great oxygen storage and release capacity due to a reversible redox reaction between Ce^{3+} and Ce^{4+} ions inside the ceria crystal lattice [17]. Ceria is also characterized by great thermal, mechanical, and chemical stability, as well as low cost and low toxicity [18]. The catalytic properties of ceria can be improved by doping, i.e., partial replacement of the cerium ions in the crystal lattice with foreign ions. Zirconium-doped ceria ($Ce_xZr_{1-x}O_2$) has been extensively investigated for its application as a catalyst in various processes, including volatile organic compounds (VOCs) catalytic combustion [19]. The introduction of Zr^{4+} ions into the ceria crystal lattice improves its oxygen storage capacity, as well as its thermal, mechanical, and chemical stability [20]. Zirconium-doped ceria is used as a catalyst and catalyst support [21], but its efficiency can be constrained due to limited surface area [22], which can be significantly increased by nanocasting. Several reports describe the preparation of nanocast ceria using MCM-48 [23], SBA-15 [22,24–27], and KIT-6 templates [24,25]. Additionally, it has been shown that mesoporous ceria–zirconia solid solutions can also be prepared by nanocasting using the same types of templates, including MCM-48 [28], SBA-15 [29], and KIT-6 template [29–31]. Other ceria-based solid solutions have also recently been prepared via nanocasting [32,33]. Using KIT-6 as a template for ceria nanocasting enables the control of ceria morphology, pore volume, surface area, etc., leading to enhanced catalytic properties [34].

However, in research on the preparation of ceria by the nanocasting process, we noticed certain uncertainties and inconsistencies, particularly regarding the influence of reaction parameters, especially the hydrothermal aging temperature, on the final product. Also, the investigation of ceria–zirconia solid solution preparation using the KIT-6 template was mainly concentrated on utilization, either as a sensor or as a catalyst. Therefore, our goal was to prepare mesoporous zirconium-doped ceria by the hard template method using the KIT-6 template, investigate the influence of synthesis parameters on the template properties, use the prepared templates for the process of zirconium-doped ceria nanocasting, and, finally, investigate the properties of the product. We paid particular attention to the microstructure and texture of the prepared samples, but we also investigated the catalytic activity of the nanocast material on a model system. Toluene was selected as a model compound because it is a typical representative of VOCs, which are considered a significant threat to human health [35].

https://doi.org/10.3390/cryst16020083

2. Materials and Methods

The synthesis of KIT-6 mesoporous silica was carried out according to the procedure of Kleitz and co-workers [36]. First, 5.13 g of P123 polymer (poly-(ethylene glycol)-block-poly-(propylene glycol)-block-poly(ethylene glycol), p.a., Sigma-Aldrich, St. Louis, MO, USA), 185.33 g of distilled water and 9.93 g of 37% HCl (p.a., VWR Chemicals, Radnor, PA, USA) were added into a polypropylene bottle, and then the mixture was stirred on a magnetic stirrer at 35 °C with 500 rpm for 48 h. The polymer is then completely dissolved, and 5.13 g of 1-butanol (p.a., VWR Chemicals, Radnor, PA, USA) and 11.03 g of TEOS (tetraethylorthosilicate, p.a., Merck-Schuchardt, Hohenbrunn, Germany) are added to the reaction mixture. The mixture is stirred vigorously at 35 °C with 800 rpm for 24 h. The reaction mixture is then transferred to a dryer, where it is aged at 60, 100, or 140 °C for 48 h. The sample that has been aged at a temperature of 140 °C had to be transferred to an autoclave, while, in the case of lower temperatures, the process is continued in a tightly closed polypropylene bottle. After 48 h of aging, the reaction mixture was removed from the dryer and cooled in air, vacuum filtered using a Büchner funnel for 45 min, and dried at 140 °C for 24 h. In order to remove the template, the sample was placed in the reaction vessel along with 150 mL of ethanol and 3 drops of HCl (37%, Kemika, Zagreb, Croatia) and stirred on a magnetic stirrer for 45 min at 500 rpm. After that, the mixture was filtered again using a Büchner funnel for 45 min and dried in air for 48 h. Finally, the sample is gradually heated (2 °C min^{-1}) to 550 °C and held at that temperature for 6 h. The samples were named K6-60 (silica sample aged at 60 °C), K6-100 (silica sample aged at 100 °C) and K6-140 (silica sample aged at 140 °C)

The nanocasting process started with the degassing of the silica template in vacuum at 150 °C for 2 h. In order to prepare the nanocasted $Zr_{0.15}Ce_{0.85}O_2$, 2.26 g of cerium(III) nitrate hexahydrate ($Ce(NO)_3{\cdot}6H_2O$, p.a., Acros organics, Geel, Belgium), 0.24 g of zirconyl nitrate dihydrate ($ZrO(NO_3)_2{\cdot}2H_2O$, p.a., Reachim, Moscow, Russia) and 1 g of K6-100 silica template obtained in the previous synthesis step were used. For the K6-60 template, the salt masses were reduced to 1.8 g of $Ce(NO)_3{\cdot}6H_2O$ and 0.2 g of $ZrO(NO_3)_2{\cdot}2H_2O$, as this material has smaller pores and therefore requires less precursor to fill them. In contrast, for the K6-140 template, the masses of the salts were increased to 2.71 g of $Ce(NO)_3{\cdot}6H_2O$ and 0.29 g of $ZrO(NO_3)_2{\cdot}2H_2O$ due to its larger pore volume, which required a greater amount of precursor to fill the pores. Therefore, the approximate mass ratio of salts to template was 2 for the K6-60 template, 2.5 for the K6-100 template, and 3 for the K6-140 template. The precursors and the template were mixed and homogenized in an agate mortar with 10 mL of hexane until the hexane evaporated. Then, the powder was transferred to a 50 mL round-bottomed flask placed in an oil bath with a condenser, and an additional 30 mL of hexane was added. The mixture was stirred at 80 °C and 1200 rpm for 12 h. After mixing, the resulting product was filtered by vacuum filtration using a Büchner funnel and dried at 70 °C in a drying oven for 24 h. The product was further calcined at 500 °C for 12 h. The silica was removed by transferring the product to a plastic bottle with a stopper, together with 30 mL of NaOH (p.a., Gram Mol, Zagreb, Croatia), and stirred at 80 °C and 400 rpm in an oil bath for 24 h. The last step of the synthesis was washing the obtained product in water and ethanol. The samples were named ZC-60 ($Zr_{0.15}Ce_{0.85}O_2$ sample aged at 60 °C), ZC-100 ($Zr_{0.15}Ce_{0.85}O_2$ sample aged at 100 °C), and ZC-140 ($Zr_{0.15}Ce_{0.85}O_2$ sample aged at 140 °C).

Scanning electron microscope (SEM) micrographs were obtained using Tescan Vega 3 SEM (Tescan, Brno, Czech Republic) operating at 10 kV. Samples were fixed on specimen holders with double-sided carbon conductive tape and gold and platinum-coated using a Quorum SC 7620 sputter coater (Quorum Technologies, Laughton, UK). Energy dispersive

X-ray spectroscopy (EDS) spectra were obtained via an EDS spectrometer, Bruker Quantax Compact detector (Bruker, Billerica, MA, USA), coupled with Tescan Vega 3 SEM.

Transmission electron microscope (TEM) and scanning transmission electron microscope (STEM) micrographs were obtained using a Jeol (Tokyo, Japan) probe Cs corrected ARM 200 CF scanning transmission electron microscope with an accelerating voltage of 80 kV coupled with a Jeol Centurio 100 EDS detector providing elemental mapping.

Small-angle X-ray scattering (SAXS) patterns were measured by using an X-ray diffractometer X'Pert Pro (Malvern Panaalytical, Malvern, UK) with CuKα radiation, and the scanning angle was from 0.5 to 8°2θ with a step of 0.026°2θ.

X-ray diffraction (XRD) analyses were conducted using a Shimadzu XRD 6000 (Tokyo, Japan) diffractometer with CuKα radiation at a voltage of 40 kV and a current of 30 mA. The diffraction patterns were obtained in step mode in the angle range from 5 to 105°2θ with a step of 0.02°2θ and a dwell per step of 0.6 s. Crystallite sizes were calculated using the Scherrer equation [37]: $d = k\lambda/\beta cos\theta$, where d is the crystallite size expressed in nm, k is a constant dependent on the crystal system and equals 0.94 for spherical crystallites of cubic symmetry, λ is the wavelength of CuKα radiation which is 0.15405 nm, θ is the Bragg angle of the diffraction maximum, and β is the half-width of the corresponding diffraction maximum corrected for instrumental broadening. The instrumental broadening was taken as the half-width of the (220) diffraction maximum of the cerium(IV) oxide sample annealed at 1200 °C for 2 h (0.16°2θ). The Zirconia share was calculated via normalized reference intensity ratio (RIR) method [38], which in this specific case reads as follows: $\mathrm{w_{ZrO2} = I_{ZrO2}/RIR_{ZrO2}[1/(I_{ZrO2}/RIR_{ZrO2} + I_{CeO2}/RIR_{CeO2})}$, where $\mathrm{I_{ZrO2}}$ and $\mathrm{I_{CeO2}}$ are measured intensities of ZrO_2 and CeO_2 diffraction maxima with the greatest intensity and $\mathrm{RIR_{ZrO2}}$ and $\mathrm{RIR_{CeO2}}$ are reference intensity ratios of corresponding phase read from ICDD PDF.

Fourier-transformed infra-red spectroscopy (FTIR) analysis was performed on a Fourier-transformed infra-red spectrometer, Bruker Vertex 70 (Bruker Optics, Karlsruhe, Germany), using attenuated total reflection (ATR). The samples were pressed onto a diamond, and the absorbance was recorded in the range between 400 and 5000 $\mathrm{cm^{-1}}$ with a spectral resolution of 2 $\mathrm{cm^{-1}}$ and 32 scans.

N_2 adsorption-desorption isotherms were recorded on a ASAP-2000 device (Micromeritics, Norcross, GA, USA) at 77 K. The samples were previously degassed at 100 °C in a dynamic vacuum of 7 mPa. The Barrett–Joyner–Halenda method [39] was used to obtain pore size, while the SSA was determined by the Brunauer–Emmett–Teller (BET) method [40].

UV-Vis diffuse reflection spectroscopy was performed with an Ocean Insight QE Pro High-Performance spectrometer (Ocean Optics, Orlando, FL, USA) equipped with an integrating sphere for reflection, while $BaSO_4$ was used as a standard. The measured spectra are transformed into Kubelka-Munk functions [41]: $F(R_\infty) = (1 - R_\infty)^2/2R_\infty$, where $F(R_\infty)$ is the Kubelka–Munk function that is proportional to the absorption coefficient (α), and R_∞ is the reflectance of an infinitely thick sample and is calculated according to the formula: $R_\infty = R_{\mathrm{sample}}/R_{\mathrm{standard}}$. The bandgap ($E_g$) is determined from Tauc's graphic representation of the dependence of $[F(R)h\nu]^{\mathrm{n}}$ on the photon energy ($E = h\nu$), where n is 2 for a direct and ½ for an indirect semiconductor, h is the Planck's constant, and ν is frequency defined as the ratio of the speed of light (c) and the wavelength of light radiation of the spectrometer (λ) [41]. The linear part of the obtained curve is extrapolated on the abscissa, from which it is possible to read the energy corresponding to the bandgap.

A WITec alpha300 Raman spectrometer (Oxford Instruments, Ulm, Germany) with a 532 nm laser was used for the measurements. At the start of the measurements, the spectrometer was calibrated using a Si sample measured at 520 $\mathrm{cm^{-1}}$. Raman spectra were

https://doi.org/10.3390/cryst16020083

recorded at room temperature. The laser power was set to 10 mW. Spectra were recorded with a 50× objective.

The catalytic activity of zirconium-doped cerium(IV) oxide samples was tested in a process of catalytical degradation of toluene as a model volatile organic compound. An integral up-flow fixed-bed reactor with 7 mm internal diameter at atmospheric pressure was used for testing. Inside the reactor 50 mg of powdered catalyst was placed between two quartz wool plugs. Quartz inserts were placed at both ends of the catalyst bed in order to avoid dead volume in the reactor and to preheat the reaction mixture to the operating temperature. A 242 ppm mixture of toluene with nitrogen (Messer Croatia Plin, Zaprešić, Croatia) was passed through the reactor at a volumetric flow rate of 80 cm^3 min^{-1}. Air was used as an oxidant (SOL Group, Monza, Italy) with a volume flow rate of 12 cm^3 min^{-1}. The flow rates were regulated by mass flow controllers MFC 4800 Series (Brooks, Hartfield, VA, USA), while the reactor temperature was controlled by a thermocontroller TC208 series (Brooks, Hartfield, VA, USA) connected to a thermocouple located inside the reactor and a heater around the reactor. An online gas chromatograph GC-2014 (Shimadzu, Tokyo, Japan) equipped with a flame ionization detector (FID) and a RTX-WAX (Restek; supplied by AnAs d.o.o., Zagreb, Croatia) capillary column (1 µm) was used to determine the concentration of toluene in the reactor effluent.

3. Results and Discussion

SEM micrographs of prepared KIT-6 samples are shown in Figure 1a–c. The microstructures of the prepared samples are quite similar. All three samples consist of heavily aggregated particles of irregular shapes and dimensions, mostly below 10 µm. Such microstructure can be rated as common for sol-gel-derived silica materials prior to thermal treatment. The EDS spectra of the samples (Figure 1d) show that the samples consist only of Si and O, indicating high purity.

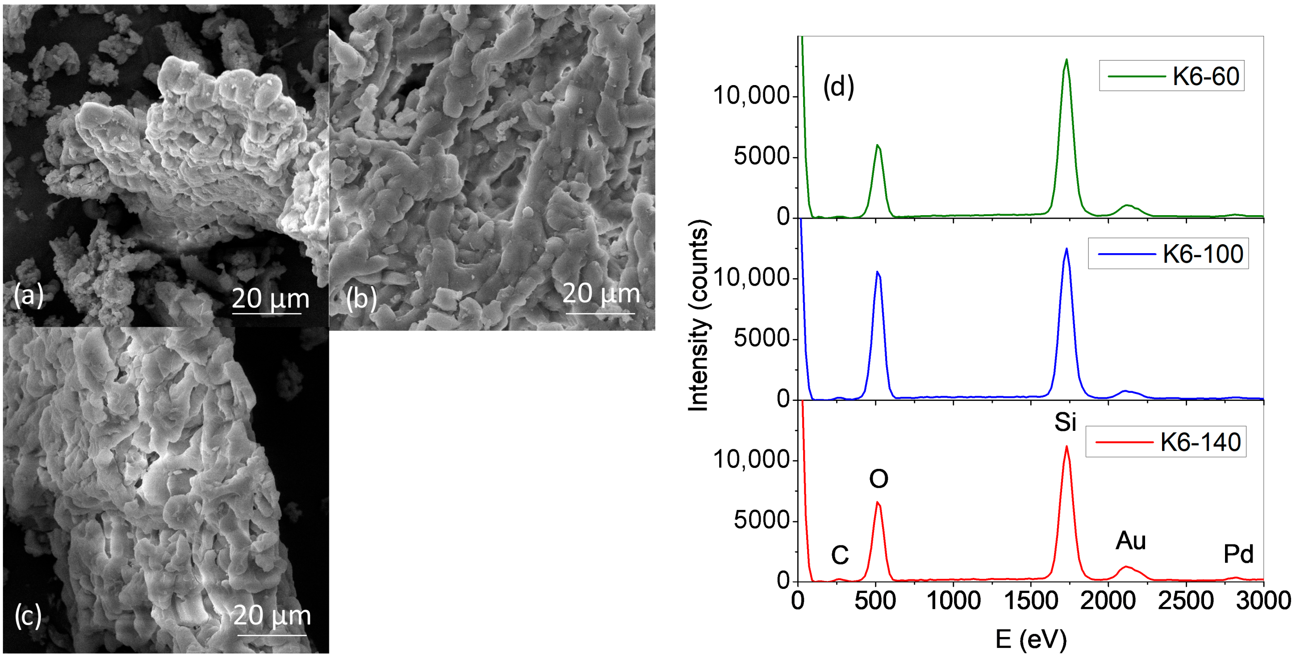

Figure 1. SEM micrographs of samples (**a**) K6-60, (**b**) K6-100, and (**c**) K6-140. (**d**) EDS spectra of KIT-6 samples aged at different temperatures.

Periodicity of uniform mesoporous materials could be investigated via X-ray scattering methods, and porous networks could be associated with certain structures and reflections related to planes with Miller indices [42]. Figure 2a shows the small-angle X-ray scattering pattern of the sample KIT-6 aged at 100 °C. The presence of low-angle diffraction peaks indicates that the sample possesses an ordered mesoporous network. Since KIT-6 possesses cubic *Ia*¯3*d* symmetry [43], peaks could be indexed as (211), (220), and (332). Therefore, the existence of an ordered 3D mesoporous silica structure is confirmed. The reflex occurring at 0.87° (2θ) could, through the Bragg equation, be related to planes 10.1 nm apart. As can be observed in the XRD patterns (Figure 2b), no reflections at higher angles are observed except the so-called amorphous halo at ~22.5°2θ, related to amorphous silica [44]. Thus, mesostructured and amorphous silica has been prepared.

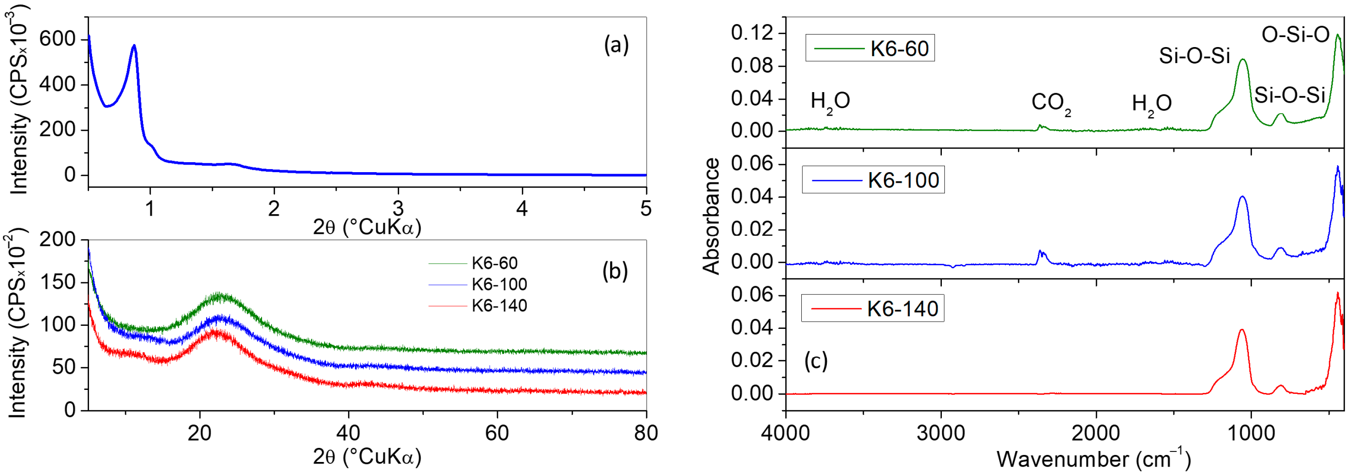

Figure 2. (**a**) Low-angle XRD pattern; (**b**) wide-angle XRD pattern of sample K6-100; (**c**) FTIR spectra of KIT-6 samples aged at different temperatures.

The FTIR spectra of the prepared KIT-6 samples are shown in Figure 2c. The bands at ~1060 cm^{-1} and ~810 cm^{-1} are due to asymmetric and symmetric stretching Si-O-Si vibrations, respectively, while the band at ~440 cm^{-1} is due to the O-Si-O bending mode [45,46]. Very weak and broad band in the 3700–2700 cm^{-1} interval and a faint band at ~1660 cm^{-1} visible in spectra of samples K6-60 and K6-100 correspond to adsorbed water [43], while bands at ~2340 and 2360 cm^{-1} are attributed to adsorbed CO_2 [47].

Isotherms and pore size distributions of the KIT-6 samples hydrothermally aged at different temperatures are shown in Figure 3. The shapes of all three isotherms are of type IVa, with a characteristic final saturation plateau, where capillary condensation is accompanied by hysteresis of type H1 according to IUPAC [48]. The shape of the isotherms indicates mesoporous materials with small pores, which is in concordance with the determined average pore size (Table 1). The shape of loops is related to the geometry of pores, where H1 type indicates predominant cylindrical geometry [48]. The narrowness of the loops indicates uniform pore size. The observed isotherms are quite typical for KIT-6 material, which usually exhibits an ordered 3D network of open cylindrical pores. Hysteresis loops of investigated samples begin roughly at relative pressures of approximately 0.45, 0.55, and 0.65, with substantial N_2 uptake up to p/p_0 of 0.80, 0.90, and 0.95 for the samples of the K6-60, K6-100, and K6-140, respectively. This shift indicates an increase in pore diameter with increasing aging temperature.

Average pore diameter (Table 1) indeed increases from 4.1 nm for the sample aged at 60 °C, 5.8 nm for the sample aged at 100 °C, to 8.4 nm for the sample aged at 140 °C. The observation of an increase in pore size of KIT-6 samples with aging temperature is consistent with the literature [7,11,49]. Pore size distribution is monomodal and relatively narrow (Figure 3b). However, a certain broadening is noted for the sample aged at 140 °C, which could be a consequence of pore collapse and agglomeration [11]. The increase in pore volume and the decrease in wall thickness are interrelated. Therefore, high hydrothermal temperatures lead to structural degradation of the porous material [49].

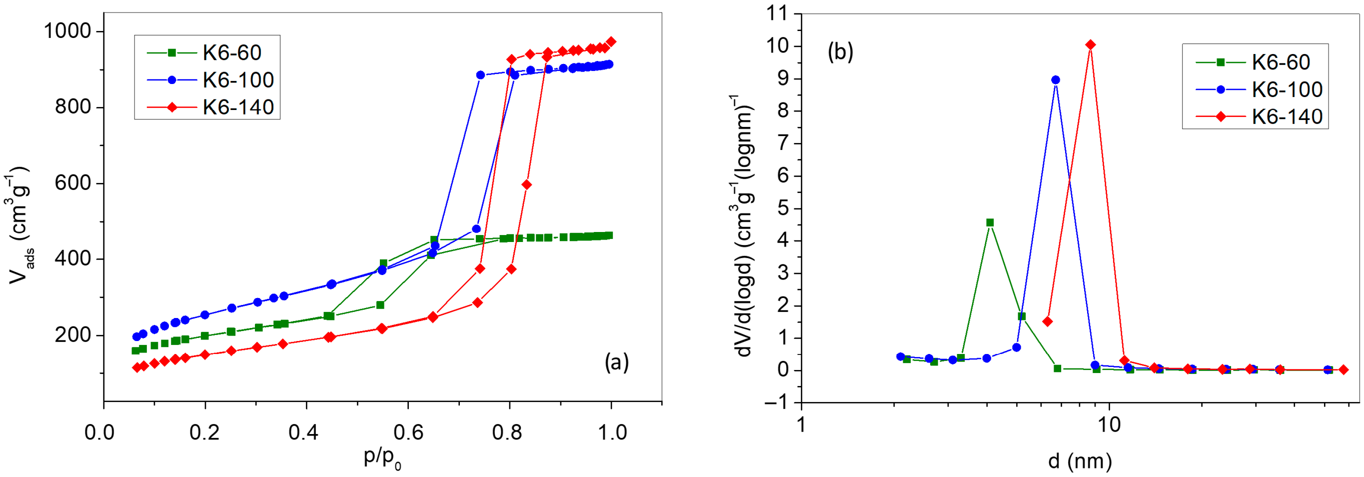

Figure 3. (**a**) N_2 adsorption/desorption isotherms; (**b**) pore size distributions of KIT-6 samples aged at different temperatures.

Table 1. SSA and pore characteristics of KIT-6 samples aged at different temperatures.

Sample	BET Specific Surface Area ($m^2\ g^{-1}$)	BJH Desorption Average Pore Diameter (nm)	BJH Cumulative Desorption Pore Volume ($cm^3\ g^{-1}$)
K6-60	711	4.1	0.768
K6-100	925	5.9	1.449
K6-140	546	8.4	1.492

SSA (Table 1) increases from the sample aged at 60 °C (711 $m^2\ g^{-1}$) to the sample aged at 100 °C (925 $m^2\ g^{-1}$). Although the average pore diameter decreased with increasing aging temperature, a notable increase in pore volume was observed, indicating the formation of a larger number of pores. This was further supported by the increase in SSA. However, when the aging temperature was increased to 140 °C, the SSA decreased to 546 $m^2\ g^{-1}$, suggesting partial collapse or restructuring of the pore network at higher temperatures. Considering the increase in pore size with aging temperature and the same pore volume, one should expect the decrease in SSA, as occurred for material aged at 140 °C in relation to material aged at 100 °C. The growth of pores results in a reduction in the surface-to-volume ratio, and thus the total surface area of the material is reduced. On the other hand, the increase in SSA for material aged at 100 °C with respect to material aged at 60 °C is a consequence of better mesostructural organization of the material. This is evident from the cumulative pore volume, as a substantial increase in the adsorbed volume is observed when comparing the sample aged at 60 °C (0.768 cm^3g^{-1}) with the one aged at 100 °C (1.449 cm^3g^{-1}). On the other hand, an almost negligible increase in adsorbed volume was observed for the sample aged at 140 °C (1.492 cm^3g^{-1}). According to Zhou et al. [11], this is a consequence of the increase in pore diameter, which reduces the pore-wall thickness and makes the collapse of the pore walls more likely.

Figure 4a,b present STEM micrographs of the KIT-6 sample aged at 100 °C showing an ordered porous architecture with uniformly distributed pores. On the far-left side of Figure 4a, a three-dimensional arrangement of pores can even be discerned. A typical regular hexagonal arrangement of pore ends with uniform size distribution can be observed in Figure 4b. The plane shown is consistent with the view along the [111] direction [50]. Dark spots in STEM-ADF micrographs correspond to areas with lower material density/thickness, i.e., the pores, while bright areas correspond to areas with higher density of material, i.e., the silica framework. The pore diameters and pore wall thickness could be roughly assessed to be 6 and 3 nm. If these two numbers are added together, a value of 9 nm is obtained, which is close to the 10.1 nm distance of planes calculated from SAXS peak position (Figure 2a) through the Bragg equation.

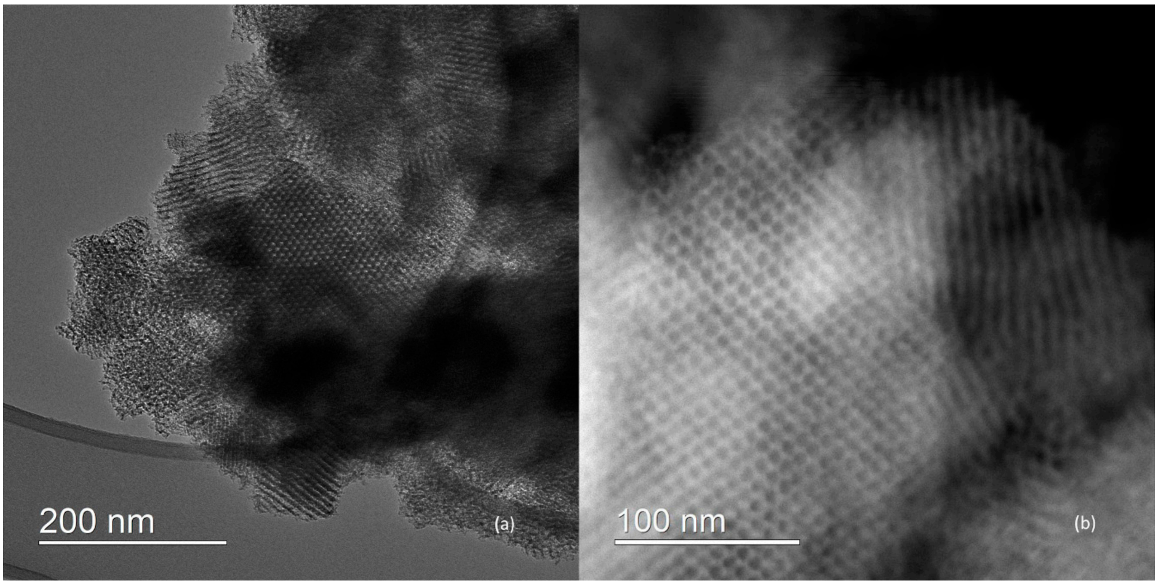

Figure 4. (**a**) STEM-BF; (**b**) STEM-ADF micrographs of the sample K6-100.

Figure 5a–c present SEM micrographs of mesoporous Zr-doped ceria obtained by nanocasting using KIT-6 templates aged at different hydrothermal aging temperatures. An aggregate of smaller particles, which can be inferred to be rod-shaped, could be observed in Figure 5a,b. Figure 5d–g show the results of EDS mapping. As can be observed, the distribution of Ce and Zr is uniform, which indicates the formation of a solid solution.

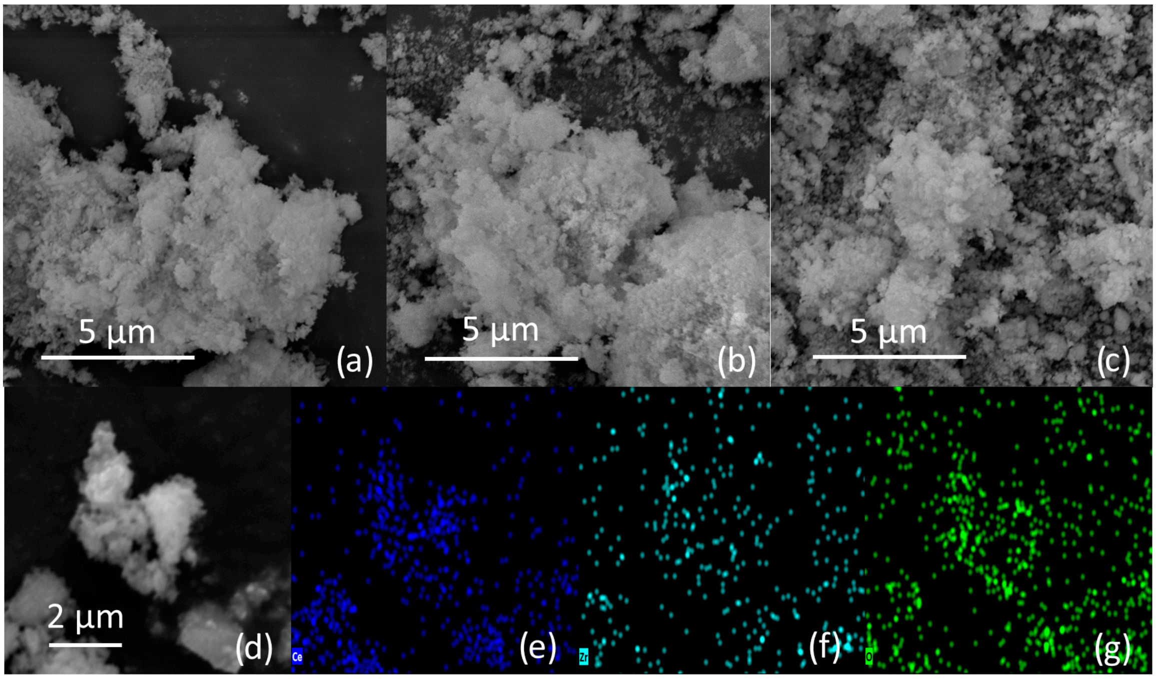

Figure 5. (**a**) SEM micrographs of samples (**a**) ZC-60, (**b**) ZC-100, and (**c**) ZC-140, (**d**) SEM micrograph of sample ZC-100, and corresponding EDS elemental mapping images of (**e**) Ce, (**f**) Zr, and (**g**) O.

https://doi.org/10.3390/cryst16020083

In the TEM micrograph (Figure 6a), ordered, rod-shaped formations can be well distinguished. However, rods are relatively short, and it is hard to tell how much of the 3D microstructure has been preserved in the replication process. On the basis of TEM micrographs, it seems more plausible that the 3D structure has collapsed to a 1D structure. The pores were likely only partially filled with the mixed metal oxide precursors, and after template removal with the NaOH solution, the replica could only partially retain its original mesostructural symmetry. The possible reason for this is the decrease in precursor concentrations by the end of the template filling process, and thus, limited diffusion into the remaining free pore space [51]. The same could be the consequence of volume shrinkage in the course of calcination [52]. If the filling is low, the material within the template is segmented, and the 3D network cannot be maintained after the template removal, yielding separated nanorods. The rods look segmented, as if they were sporadically assembled from particles of irregular shape. The size of such particles, as well as the diameter of the rods, can be estimated to be between 5 and 7 nm. That is roughly in concordance with the BJH pore diameter of K6-100, as expected since the particles were formed in a confined space of silicon template pores. Similar nanorod size (8–10 nm) of zirconium-doped ceria has been reported by Abdollahzadeh Ghom et al. [29], who also conclude that these are due to growth limitations imposed by the template. HRTEM micrograph at higher magnification (Figure 6b) reveals particles with differently oriented fringes, indicating random orientation of particles. The measured interlayer distance of 0.304 ± 0.004 nm is consistent with the (111) crystallographic plane of the ceria structure. Due to their lowest surface energy, the appearance of {111} planes is most common for ceria nanoparticles [53].

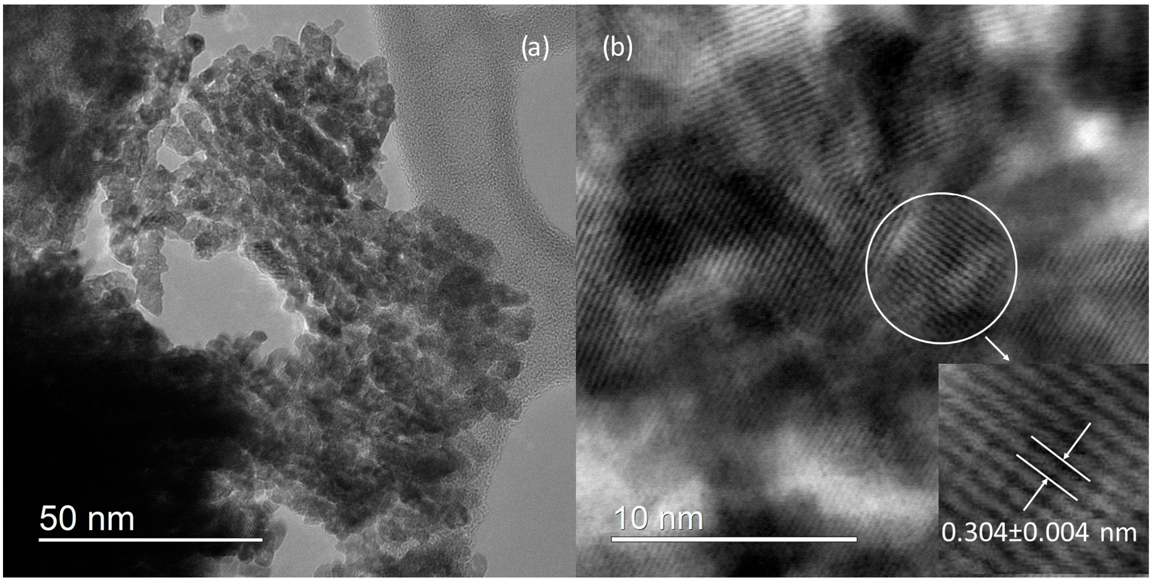

Figure 6. (**a**) HRTEM micrograph of sample ZC-100; (**b**) HRTEM micrograph of sample ZC-100 under greater magnification revealing fringes.

Figure 7a shows XRD patterns of the prepared Zr-doped ceria nanocast samples. Diffraction peaks of ceria, CeO_2, having a cubic fluorite structure (ICDD PDF No. 34-394), dominate the pattern. However, very small peaks corresponding to cubic zirconia, ZrO_2 (ICDD PDF No. 89-9069), can also be detected. The ionic radius of the Ce^{4+} ion is 97 pm, while the ionic radius of the Zr^{4+} ion is 84 pm [54], so the entrance of zirconium into the crystal lattice of ceria should cause a small decrease in the lattice constant. The calculated ceria lattice constants for all three samples (Table 2) are slightly smaller than for pure ceria (a = 5.4110 Å, according to the ICDD PDF No. 34-394). Therefore, it is reasonable to conclude that lattice shrinkage is the consequence of $Zr_xCe_{1-x}O_2$ solid solution formation.

However, due to the appearance of a secondary zirconia phase, the zirconium content in ceria is below 15%.

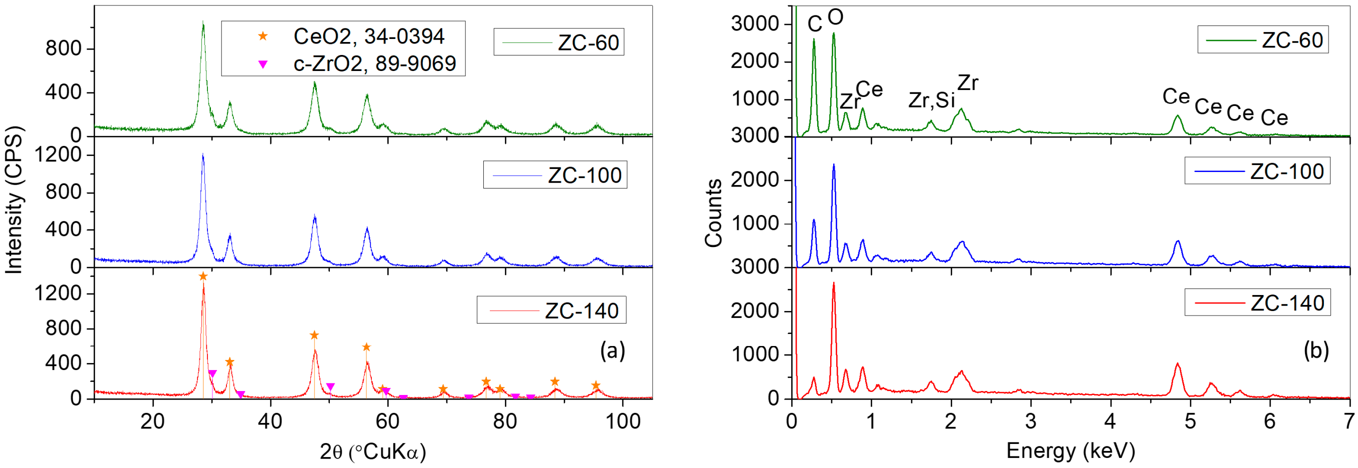

Figure 7. (**a**) X-ray diffraction patterns; (**b**) EDS spectra of investigated nanocast samples.

Table 2. Ceria lattice constant and crystallite size and zirconia share in the prepared samples.

Sample	Ceria Lattice Constant (Å)	Ceria Crystallite Size (nm)	Zirconia Share (wt. %)
ZC-60	5.4017 ± 0.0002	8.0 ± 0.4	2.1
ZC-100	5.3973 ± 0.0002	9.3 ± 0.5	1.5
ZC-140	5.3986 ± 0.0002	9.6 ± 0.5	-

The broad diffraction peaks indicate a small size of the ceria crystallites. Therefore, average crystallite sizes were calculated using the Scherrer equation and given in Table 2. Judging by the grain size calculated from TEM micrographs, the obtained crystallite sizes are slightly overestimated because crystallite size should not be greater than grain size. The discrepancy with KIT-6 pore sizes also points to overestimation. However, there is an apparent trend of an increase in crystallite size with KIT-6 template aging temperature. Of course, after the salts enter the pores, solvent evaporation is followed by salt decomposition and oxide formation at the thermal treatment temperature. In any case, the prepared catalysts are small enough to provide a high density of catalytically active sites when used as catalysts [55]. The Zirconia share was calculated using the RIR method and given in Table 2. The zirconia peak for sample ZC-140 was too small to be fitted, and thus, the share could not be calculated. The method is not considered particularly accurate, but it can be observed that the zirconium content is not significant. Based on this data, it could be concluded that the majority of zirconium entered the ceria crystal lattice.

EDS spectra of investigated samples (Figure 7b) show peaks of cerium (Ce), zirconium (Zr), and oxygen (O) at their respective energies, confirming the presence of elements in concordance with the XRD patterns. A carbon peak is present due to the use of a carbon conductive adhesive tape to mount the sample and possibly from adventitious contamination during sample preparation and analysis. The spectrum also indicates the presence of traces of silicon from the template. Si presence was confirmed via FTIR spectroscopy.

Figure 8 shows the N_2 adsorption-desorption isotherms and pore size distributions of the investigated nanocast samples. The SSAs and pore characteristics are displayed in Table 3. As can be observed, the aging temperature of the KIT-6 template affected the texture properties of nanocast replicas. However, the differences are not so significant. The template aged at 60 °C had the smallest pore diameter. Metal oxide grows inside the pores, and the pore diameter limits the size of the formed nanorods. Therefore, the sample obtained using the template with the smallest pore diameter will contain nanorods with the smallest diameter and, consequently, exhibit the greatest SSA. Afterward, when the template is removed with NaOH, the initial mesostructure is destroyed, and the nanorods are released. Due to a series of subsequent processes, the final nanorod dimensions may become larger than the original KIT-6 pore sizes, but the initial differences are preserved to some extent. Thus, the SSA of the nanocast oxide decreases with increasing pore diameter of the KIT-6 template. In addition to nanorod diameter, the SSA is also influenced by the crystalline nature and the higher bulk density of metal oxides compared with silica [56], both of which reduce the SSA of all nanocast samples. The obtained SSAs are roughly in the range of literature values for similar systems, being in the range between 101 and 139 m^2g^{-1} [28–31]. However, it is difficult to compare the obtained SSA values with the values reported in literature due to differences in the template used, zirconia share, preparation details, and heat treatment temperature. The pore volume is reduced, and the pore size distribution shifts toward the macroporous region. In this case, the pore volume and pore diameter of the nanocast samples do not refer to ordered mesostructure, as they were for the template, but rather to the interparticle voids, as can be observed in Figure 6a. As particles become larger, the average pore diameter decreases slightly, while the pore volume decreases substantially. This behavior results from the development of a bimodal pore size distribution within the aggregates (Figure 8b, ZC-140). The larger proportion of smaller pores resulted in a decrease in pore volume and a shift of the pore size distribution toward smaller values compared to samples ZC-60 and ZC-100. N_2 adsorption-desorption isotherms can again be rated as type IV, but the hysteresis loops resemble the H3 type this time. The same was reported by Yang et al. [30] for KIT-6-derived mesoporous zirconium-doped ceria. The H3 loop is typically associated with slit-shaped pores [22,57]; however, in this case, it is a consequence of voids within aggregated particles and pores between particles [58]. The space where capillary condensation occurs is not rigid, and porosity is poorly defined.

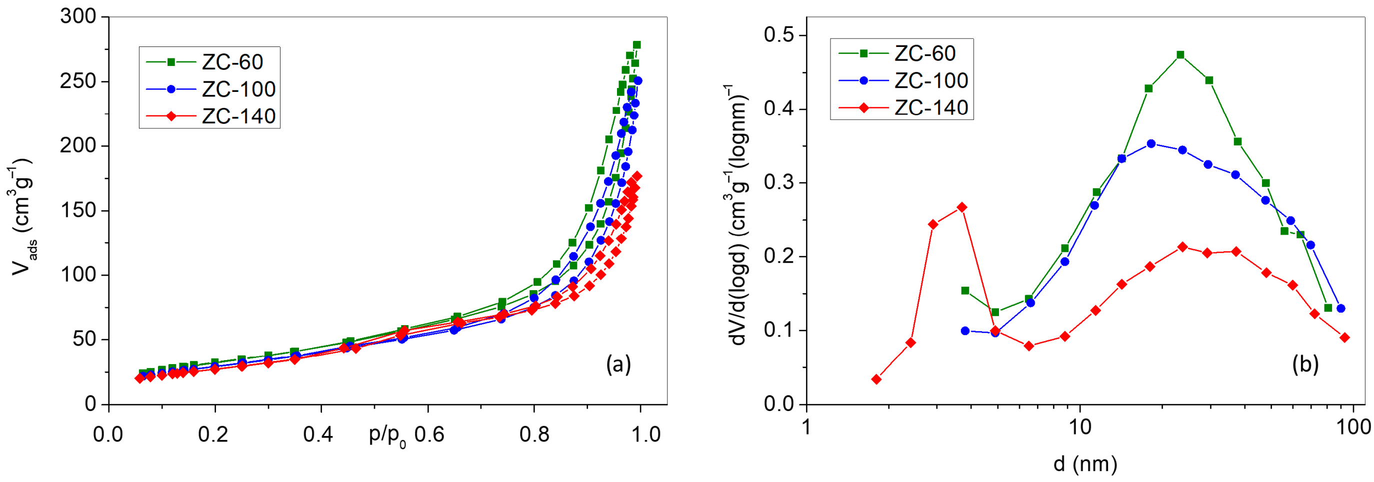

Figure 8. (**a**) N_2 adsorption/desorption isotherms; (**b**) pore size distributions of investigated nanocast samples.

Table 3. SSA and pore characteristics of investigated nanocast samples.

Sample	BET Specific Surface Area (m^2 g^{-1})	BJH Desorption Average Pore Diameter (nm)	BJH Cumulative Desorption Pore Volume (cm^3 g^{-1})
ZC-60	120	11.1	0.422
ZC-100	107	11.1	0.378
ZC-140	99	8.0	0.270

The UV-Vis absorption spectra of Zr-doped ceria nanocast samples are shown in Figure 9a. The absorption spectra exhibit strong absorption in the UV area and complete reflectance in the Vis spectrum area. The absorption in the UV region is due to charge transfer transitions between the O^{2-} (2p) and Ce^{4+} (4f) orbitals [20]. Although reflectance values above 100% are physically unrealistic, they can be observed when luminescence contributes additional emitted light to the detected signal [59]. From the absorption data, the bandgap energy (E_g) was calculated using Tauc's equation. Ceria is generally considered a direct band semiconductor, so the bandgap was calculated by plotting $(F(R)E)^2$ vs. E, where the linear region's x-intercept gives the bandgap energy, E_g. Tauc's plots for the direct bandgap are given in Figure 9b, which reveal that bandgaps of all three samples are in the range between 3.25 and 3.32 eV. Values of the CeO_2 bandgap reported in literature differ, but the value of 3.2 eV [60] appears most often. Therefore, the bandgap values are slightly blueshifted in comparison to pure ceria. The literature most often reports that zirconium entrance in ceria crystal lattice tends to redshift the ceria bandgap [20,61], although it is possible to find alternative opinions [62]. However, blueshift in the present case is most probably the consequence of the quantum confinement effect [63,64]. Quantum confinement effect is expected when dimensions are smaller or comparable with the Bohr exciton radius [65]. In the case of ceria, the Bohr radius is about 7 nm [66], which is comparable to the observed particle size of 5 to 7 nm. However, even a weak confinement regime could cause such a small blueshift as reported here.

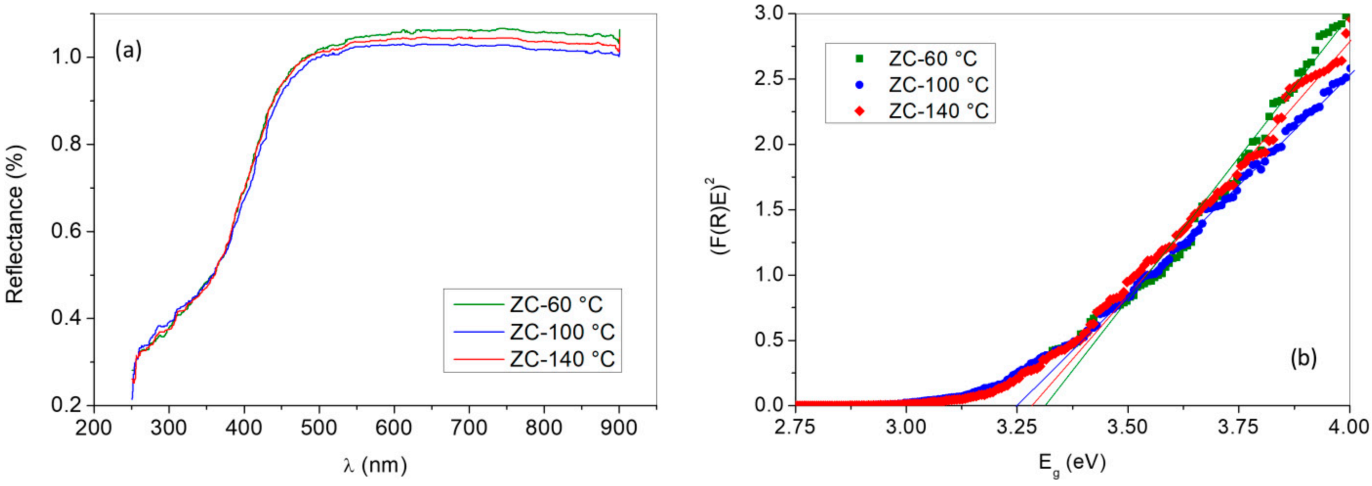

Figure 9. (**a**) Reflectance spectra; (**b**) Tauc's plots of investigated nanocasted samples.

The catalytic performance of the prepared catalysts in the toluene oxidation was investigated using a fixed-bed reactor. The influence of temperature on conversion is shown in Figure 10a. Since the tested catalysts have a completely identical composition, one would expect that the SSA would have a decisive influence on the catalytic activity. However, it turned out to be just the opposite; the sample ZC-140, having the smallest SSA, shows the greatest catalytic activity. The differences are relatively small but confirmed with additional measurements. The same sample also has the smallest pore diameter and volume, which should also lead to lower catalytic activity. The only factor in favor of the catalytic activity of this sample would be the bimodal pore size distribution, where larger pores endorse mass transport, while smaller pores comprise active sites. However, that is hardly relevant if pore volume and SSA are small.

https://doi.org/10.3390/cryst16020083

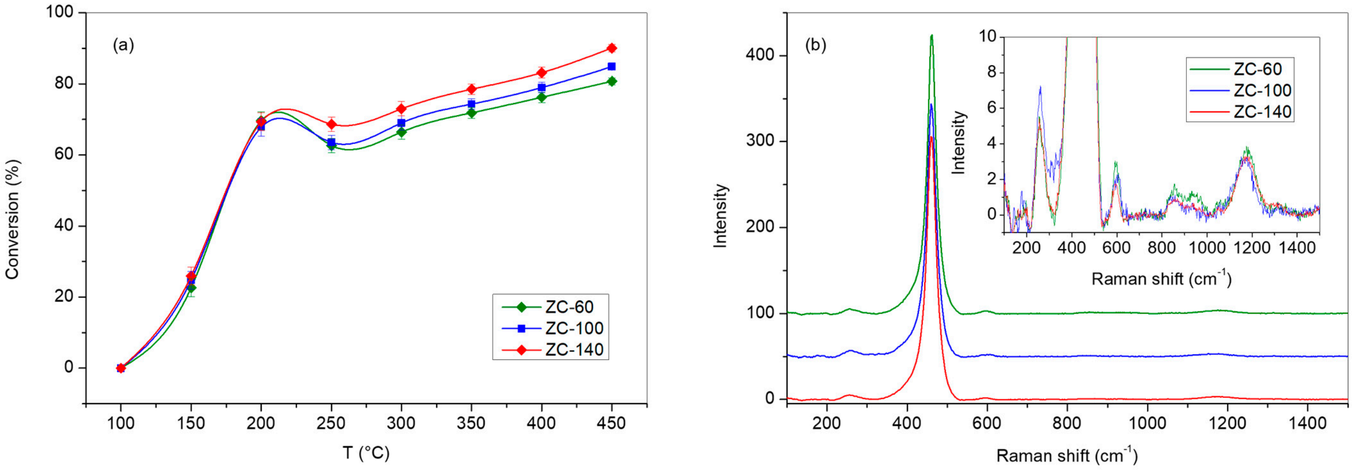

Figure 10. (**a**) The influence of temperature on the conversion of toluene over Zr-doped ceria catalysts. (**b**) Raman spectra of the investigated samples.

In order to shed more light on this phenomenon, Raman spectroscopic analysis of the investigated samples (Figure 10b) was performed. As can be observed, the spectra are dominated by the band at ~460 cm^{-1}. In addition, faint bands at ~255, ~600, and ~1180 cm^{-1} are observed (inset in Figure 10b). The sharp band at 460 cm^{-1} is attributed to symmetrical stretching vibration of oxygen ions around Ce^{4+} cation in CeO_8 octahedra in fluorite ceria structure (F_{2g} mode) [67–71]. Literature reports on a certain shift of this band in zirconium-doped ceria toward higher wavenumbers due to a replacement of greater ceria Ce^{4+} cations with smaller Zr^{4+} cations. However, no shift of this band in comparison with the value reported for pure ceria can be observed [69]. Broadening of this band due to doping with zirconium has also been reported [72]. The location of band at 600 cm^{-1} fits second-order transverse (2TO) mode, but this attribution has been ruled out [69], and in recent literature this band is attributed to the lattice ceria defects [69], i.e., substitution of Ce^{4+} with Ce^{3+} in cubic structure and the presence of corresponding intrinsic oxygen vacancies, and, in the case of zirconium doped ceria, to the replacement of Ce^{4+} ions with Zr^{4+} ions, resulting in a distortion of the cubic structure [67,68,72]. Abdollahzadeh Ghom et al. [29] also notice the presence of Ce^{3+} in mesoporous zirconium-doped ceria through XPS measurements. Yang et al. [30] have a similar weak band at ~600 cm^{-1}, but they do not comment on it. The band at 255 cm^{-1} is associated with the CeO_2 surface [69,73], and it has been noted that it increases with the decrease in ceria particle size [73]. Weak band at 1180 cm^{-1} is attributed to second-order longitudinal (2LO) mode [69,73].

No significant differences in intensity of Raman bands, particularly those attributed to lattice or surface defects, have been observed. The intensities of the 600 cm^{-1} band relative to the dominant sharp 460 cm^{-1} band are approximately 1.7, 1.6, and 1.1% for samples ZC-60, ZC-100, and ZC-140, respectively. Taking into consideration the uncertainty of intensity determination and small differences, it is not possible to draw quantitative conclusions. Therefore, the differences in catalytic activity among the investigated samples could not be attributed to variations in lattice or surface defects, i.e., sites where oxygen could be uptaken and subsequently released. Crystallite size as well as the amount and phase distribution of zirconia were also considered. Sample ZC-140, showing the greatest catalytic activity, has the greatest crystallites, so crystallite size is clearly not a factor relevant to catalytic activity. Quantitative analysis showed the lowest amount of zirconia in sample ZC-140, but the zirconia quantity is small in all samples, and the differences are not substantial. Therefore, neither the amount nor the distribution of zirconia could be related to catalytic activity.

So, we turned to another oddity in the appearance of conversion curves in the hope that it could contribute to the understanding of the behavior of the investigated catalysts. Namely, all curves have a segment that seems to represent the deceleration of the reaction rate in the range between 250 and 300 °C. Strong arguments have been made in the literature [35,57,74], stating that this phenomenon is actually a consequence of extensive toluene adsorption in the lower temperature range. The extensive adsorption of toluene gas causes a drop in the toluene concentration at the outlet, which creates the appearance of an accelerated conversion rate. As the temperature increases, toluene desorption occurs, which is measured at the outlet, creating an apparent drop in conversion. This phenomenon comes to the fore due to the relatively great SSA of the catalysts and relatively low inlet gas concentration of toluene. Process is described as being "two-stage", although the process consists of adsorption, desorption, and degradation [74], and it would be more correct to call it "three-stage". One more argument in favor of this explanation is that the sample having the greatest SSA (ZC-60) shows the greatest apparent deceleration in toluene conversion rate. This sample has the greatest SSA, and thus it is capable of adsorbing the greatest amount of toluene. On the other hand, the sample with the smallest SSA shows the smallest apparent deceleration in toluene conversion rate.

If one looks at the problem in this light, there are no real differences in the catalytic activity of the investigated catalysts. Slight differences in catalytic activity are only due to a difference in the amount of adsorbed toluene caused by the different SSA of the samples. The final results show only slight differences in apparent conversion rates.

Some other explanations of this unusual dependence of toluene conversion on reaction temperature could be found. First is the change in the reaction mechanism where the process control switches between intrinsic oxidation rate and reactants mass transfer, which we found improbable in this particular case because it would require the decrease in diffusion rate with temperature in one step of the process. Another explanation relies on the stability of intermediate products. At lower temperatures, initial toluene oxidation begins with the adsorption of toluene on active centers and the removal of hydrogen atoms from the methyl group by the surface lattice oxygen, thus leading to oxygen surface depletion. In the course of toluene oxidation, one of the intermediates is benzoic acid [75]. Unlike other intermediates, benzoic acid is relatively stable, and its oxidation requires a higher reaction temperature. Until a higher temperature is reached, benzoic acid accumulates on the catalyst surface, causing catalyst deactivation [76]. When, owing to temperature increase, benzoic acid oxidation is facilitated, the overall process of toluene oxidation continues.

Reasoning by Occam's razor principle, an explanation based on extensive toluene adsorption in the lower temperature range seems the most plausible. Unfortunately, in order to confirm or reject any of the hypotheses mentioned, an investigation involving modification of the setup for the catalytic experiment and online oxidation products analysis should be conducted.

4. Conclusions

Ordered mesoporous KIT-6 samples were prepared at hydrothermal aging temperatures of 60, 100, and 140 °C. The samples consist of pure amorphous silica and possess a 3D ordered mesoporous structure with pores between 4.1 and 8.5 nm. The diameter of the mesostructured material pores increases with aging temperature. The prepared templates were utilized for Zr-doped ceria nanocasting followed by thermal treatment at 500 °C. The ordered 3D structure has collapsed, leaving behind nanorods with a diameter roughly in concordance with the corresponding KIT-6 template pore diameter. Samples are composed of nanocrystalline ceria with a small amount of cubic zirconia. However, the entrance of a certain amount of zirconium in the ceria crystal lattice has been confirmed with the decrease in the ceria lattice parameter with respect to bulk ceria. The pore diameter of the KIT-6 template decisively determines the diameter of the nanorods, and in turn, the specific surface area of the nanocast samples, which ranged between 99 and 120 m^2 g^{-1}. The space between the nanorods is not rigid, and porosity is poorly defined. Ceria bandgap values were slightly blueshifted (3.25–3.32 eV) in comparison to bulk ceria, which is most probably the consequence of quantum confinement. The presence of ceria oxygen vacancies has been established but without notable differences between samples. The catalytic performance of the prepared catalysts was tested in toluene oxidation. The conversion curves have three stages: acceleration below 250 °C due to toluene adsorption in addition to catalytic degradation, apparent stagnation or deceleration in the temperature range between 250 and 300 °C, which is a consequence of toluene desorption above 250 °C, and, finally, acceleration at temperatures above 300 °C due to toluene catalytic degradation only. Slight differences in catalytic activity are only due to a difference in the amount of adsorbed toluene caused by the different SSA of the samples.

Author Contributions: Conceptualization, K.M. and S.K.; methodology, K.M. and S.K.; validation, K.M. and F.C.; formal analysis, K.M., F.C. and F.B.; investigation, K.M., J.-S.P., F.C., F.B., G.D., L.M. and G.M.; resources, V.T. and S.K.; data curation, K.M., F.C. and S.K.; writing—S.K.; writing—review and editing, K.M., G.D., L.M., G.M., V.T. and S.K.; visualization, G.D., G.M. and S.K.; supervision, S.K.; project administration, S.K.; funding acquisition, S.K. All authors have read and agreed to the published version of the manuscript.

Funding: This research was conducted within the framework of the project HEMCAT, financed by the European Union's NextGenerationEU fund from source 581—The recovery and resiliance mechanism in the framework of programme financing of public higher education institutions and public scientific institutes.

Data Availability Statement: The original contributions presented in this study are included in the article. Further inquiries can be directed to the corresponding author.

Acknowledgments: The support of the University of Zagreb, Faculty of Chemical Engineering and Technology, is gratefully acknowledged. K. M. sincerely thanks to F. Kleitz and his research group at the Institute of Inorganic Chemistry—Functional Materials, Faculty of Chemistry of the University of Vienna, for the hospitality and the University of Vienna for the research grant.

Conflicts of Interest: The authors declare no conflicts of interest.

References

1. Li, W.; Liu, J.; Zhao, D. Mesoporous materials for energy conversion and storage devices. *Nat. Rev. Mater.* **2016**, *1*, 16023. [CrossRef]
2. Sun, R.; Wu, Y.; Han, N.; Chen, L.; Chen, Z.; Zhao, H. Mesoporous silica-based photocatalytic materials for solar energy storage and utilization. *Carbon Energy* **2025**, *7*, e70054. [CrossRef]
3. Liong, M.; Angelos, S.; Choi, E.; Patel, K.; Stoddart, J.F.; Zink, J.I. Mesostructured multifunctional nanoparticles for imaging and drug delivery. *J. Mater. Chem.* **2009**, *19*, 6251–6257. [CrossRef]
4. Grumezescu, A.M.; Ghitulica, C.D.; Voicu, G.; Huang, K.-S.; Yang, C.-H.; Ficai, A.; Vasile, B.S.; Grumezescu, V.; Bleotu, C.; Chifiriuc, M.C. New silica nanostructure for the improved delivery of topical antibiotics used in treatment of Staphylococcal cutaneous infections. *Int. J. Pharm.* **2014**, *463*, 170–176. [CrossRef] [PubMed]
5. Perego, C.; Millini, R. Porous materials in catalysis: Challenges for mesoporous materials. *Chem. Soc. Rev.* **2013**, *42*, 3956–3976. [CrossRef]
6. Yu, X.; Williams, C.T. Recent advances in the applications of mesoporous silica in heterogeneous catalysis. *Catal. Sci. Technol.* **2022**, *12*, 5765–5794. [CrossRef]
7. Blachnio, M.; Zienkiewicz-Strzalka, M.; Derylo-Marczewska, A. Mesoporous silicas of well-organized structure: Synthesis, characterization, and investigation of physical processes occurring in confined pore spaces. *Int. J. Mol. Sci.* **2025**, *26*, 9255. [CrossRef]

8. Rizzi, F.; Castaldo, R.; Latronico, T.; Lasala, P.; Gentile, G.; Lavorgna, M.; Striccoli, M.; Agostiano, A.; Comparelli, R.; Depalo, N.; et al. High surface area mesoporous silica nanoparticles with tunable size in the sub-micrometer eegime: Insights on the size and porosity control mechanisms. *Molecules* **2021**, *26*, 4247. [CrossRef]
9. Nair, M.M.; Yen, H.; Kleitz, F. Nanocast mesoporous mixed metal oxides for catalytic applications. *Comptes Rendus Chim.* **2014**, *17*, 641–655. [CrossRef]
10. Rumplecker, A.; Kleitz, F.; Salabsa, E.-L.; Schüth, F. Hard templating pathways for the synthesis of nanostructured porous Co_3O_4. *Chem. Mater.* **2007**, *19*, 485–496. [CrossRef]
11. Zhou, B.; Li, C.; Qi, N.; Jiang, M.; Wang, B.; Chen, Z.Q. Pore structure of mesoporous silica (KIT-6) synthesized at different temperatures using positron as a nondestructive probe. *Appl. Surf. Sci.* **2018**, *450*, 31–37. [CrossRef]
12. Wang, W.; Qi, R.; Shan, W.; Wang, X.; Jia, Q.; Zhao, J.; Zhang, C.; Ru, H. Synthesis of KIT-6 type mesoporous silicas with tunable pore sizes, wall thickness and particle sizes via the partitioned cooperative self-assembly process. *Microporous Mesoporous Mater.* **2014**, *194*, 167–173. [CrossRef]
13. Kim, T.-W.; Kleitz, F.; Paul, B.; Ryoo, R. MCM-48-like large mesoporous silicas with tailored pore structure: Facile synthesis domain in a ternary triblock copolymer-butanol-water system. *J. Am. Chem. Soc.* **2005**, *127*, 7601–7610. [CrossRef] [PubMed]
14. Kurajica, S.; Minga, I.; Guliš, M.; Mandić, V.; Simčić, I. High surface area ceria nanoparticles via hydrothermal synthesis experimental design. *J. Nanomater.* **2016**, *2016*, 7274949. [CrossRef]
15. Duplančić, M.; Kurajica, S.; Tomašić, V.; Minga, I. Oxidation of toluene on hydrothermally prepared ceria nanocrystals. *Chem. Biochem. Eng. Q.* **2017**, *31*, 375–383. [CrossRef]
16. Kurajica, S.; Mužina, K.; Dražić, G.; Matijašić, G.; Duplančić, M.; Mandić, V.; Županćić, M.; Munda, I.K. A comparative study of hydrothermally derived Mn, Fe, Co, Ni, Cu and Zn doped ceria nanocatalysts. *Mater. Chem. Phys.* **2020**, *244*, 12689. [CrossRef]
17. Kurajica, S.; Ivković, I.K.; Dražić, G.; Shvalya, V.; Duplančić, M.; Matijašić, G.; Cvelbar, U.; Mužina, K. Phase composition, morphology, properties and improved catalytic activity of hydrothermally-derived manganese-doped ceria nanoparticles. *Nanotechnology* **2022**, *33*, 135709. [CrossRef]
18. Mužina, K.; Kurajica, S.; Guggenberger, P.; Duplančić, M.; Dražić, G. Catalytic activity and properties of copper doped ceria nanocatalyst for VOCs oxidation. *J. Mater. Res.* **2022**, *37*, 1929–1940. [CrossRef]
19. Mužina, K.; Kurajica, S.; Bach-Rojecky, H.; Brleković, F.; Duplančić, M. Combustion Synthesis of Zirconium-Doped Ceria Nanocatalyst. *Crystals* **2024**, *14*, 108. [CrossRef]
20. Bhabu, K.A.; Theerthagiri, J.; Madhavan, J.; Balu, T.; Muralidharan, G.; Rajasekaran, T.R. Enhanced electrochemical behavior of ceria based zirconia electrolytes for intermediate temperature solid oxide fuel cell applications. *J. Mater. Sci. Mater. Electron.* **2016**, *27*, 10980–10992. [CrossRef]
21. Trovarelli, A.; Boaro, M.; Rocchini, E.; de Leitenburg, C.; Dolcetti, G. Some recent developments in the characterization of ceria-based catalysts. *J. Alloys Compd.* **2001**, *323–324*, 584–591. [CrossRef]
22. de la Calle, Á.M.; Vizcaíno, A.J.; Carrero, A.; Calles, J.A.; Megía, P.J. Study of Mesostructured CeO_2 Synthesis via Nanocasting Using SBA-15 as a Template: Influence of the Cerium Precursor. *Int. J. Mol. Sci.* **2024**, *25*, 13016. [CrossRef] [PubMed]
23. Deeprasertkul, C.; Longloilert, R.; Chaisuwan, T.; Wongkasemjit, S. Impressive low reduction temperature of synthesized mesoporous ceria via nanocasting. *Mater. Lett.* **2014**, *130*, 218–222. [CrossRef]
24. Yen, H.; Seo, Y.; Kaliaguine, S.; Kleitz, F. Tailored Mesostructured Copper/Ceria Catalysts with Enhanced Performance for Preferential Oxidation of CO at Low Temperature. *Angew. Chem. Int. Ed. Engl.* **2012**, *51*, 12032–12035. [CrossRef] [PubMed]
25. Ruiz, M.G.; Pliego, J.A.; Franco, L.E.N.; Álvarez, C.M.; Pariente, J.P.; Guaregua, N.C.M. Synthesis and characterization of mesoporous cerium oxide catalyst for the conversion of glycerol. *J. Appl. Res. Technol.* **2018**, *16*, 511–523. [CrossRef]
26. Ke, Y.; Lai, S.Y. Comparison of the catalytic benzene oxidation activity of mesoporous ceria prepared via hard-template and soft-template. *Microporous Mesoporous Mater.* **2014**, *198*, 256–262. [CrossRef]
27. Vaja, F.; Oprea, O.; Ficai, D.; Ficai, A.; Guran, C. Synthesis of CeO_2 nanoparticles on the mesoporous silica support via nanocasting. *Dig. J. Nanomater. Biostruct.* **2014**, *9*, 187–195.
28. Jampa, S.; Luengnaruemitchai, A.; Chaisuwan, T.; Wongkasemjit, S. High potential of mesoporous ceria/ceria-zirconia synthesized via nanocasting pathway for catalytic application. *Mater. Energy Effic. Sustain. TechConnect Briefs* **2017**, *2*, 25–28.
29. Ghom, S.A.; Zamani, C.; Nazarpour, S.; Andreu, T.; Morante, J. Oxygen sensing with mesoporous ceria–zirconia solid solutions. *Sens. Actuators B Chem.* **2009**, *140*, 216–221. [CrossRef]
30. Yang, P.; Zhou, S.; Lei, J. Preparation of Ordered Mesoporous Nanocrystalline Ceria and Ceria-zirconia for Soot Oxidation. *J. Wuhan Univ. Technol. Sci. Ed.* **2016**, *31*, 113–117. [CrossRef]
31. Watanabe, K.; Miyao, T.; Higashiyama, K.; Yamashita, H.; Watanabe, M. Preparation of mesoporous ceria-zirconia supported Ni-Fe catalyst for the high-temperature water-gas shift reaction. *Catal. Commun.* **2011**, *12*, 976–979. [CrossRef]
32. Xu, F.; Wang, J.; Zhao, Y.; Lin, H.; Chen, H.; Zhang, Y.; Wei, X.; Dai, H. Catalytic performance and mechanism of toluene oxidation in high humidity over the mesoporous titania.ceria supported Pt or Pd catalysts. *Appl. Catal. A Gen.* **2025**, *699*, 120277. [CrossRef]

33. Sun, M.; Li, A.; Zhang, X.; Fei, Y.; Zhu, L.; Huang, Z. Investigation of the synergistic effects of reaction-diffusion processes in hierarchical macro-mesoporous electrodes of solid oxide fuel cells. *Chem. Eng. J.* **2025**, *512*, 162317. [CrossRef]
34. Li, L.; Han, W.; Zhang, J.; Lu, G.; Tang, Z. Controlled pore size of 3D mesoporous Cu-Ce based catalysts and influence of surface textures on the CO catalytic oxidation. *Microporous Mesoporous Mater.* **2016**, *231*, 9–20. [CrossRef]
35. Cao, Y.; Zhang, C.; Xu, D.; Ouyang, X.; Wang, Y.; Lv, L.; Zhang, T.; Tang, S.; Tang, W. Low-temperature oxidation of toluene over MnO_x-CeO_2 nanorod composites with high sinter resistance: Dual effect of synergistic interaction on hydrocarbon adsorption and oxygen activation. *Inorg. Chem.* **2022**, *61*, 15273–15286. [CrossRef]
36. Kleitz, F.; Choi, S.H.; Ryoo, R. Cubic *Ia3d* large mesoporous silica: Synthesis and replication to platinum, nanowires, carbon nanorods and carbon nanotubes. *Chem. Commun.* **2003**, *17*, 2136–2137. [CrossRef]
37. Klug, H.P.; Alexander, L.E. *X-Ray Diffraction Procedures*, 2nd ed.; John Wiley & Sons Inc.: New York, NY, USA, 1974.
38. Chung, F.H. Quantitative interpretation of X-ray-diffraction patterns of mixtures. Adiabatic principle of x-ray-diffraction analysis of mixtures. *J. App. Crystall.* **1974**, *7*, 526–531. [CrossRef]
39. Barrett, E.P.; Joyner, L.G.; Halenda, P.P. The Determination of Pore Volume and Area Distributions in Porous Substances. I. Computations from Nitrogen Isotherms. *J. Am. Chem. Soc.* **1951**, *73*, 373–380. [CrossRef]
40. Brunauer, S.; Emmett, P.H.; Teller, E. Adsorption of Gases in Multimolecular Layers. *J. Am. Chem. Soc.* **1938**, *60*, 309–319. [CrossRef]
41. Lopez, R.; Gómez, R. Band-gap energy estimation from diffuse reflectance measurements on sol-gel and commercial TiO_2: A comparative study. *J. Sol-Gel Sci. Technol.* **2012**, *61*, 1–7. [CrossRef]
42. Impéror-Clerc, M.; Albouy, P.-A. Characterization of the Structure of Mesoporous Materials by X-ray Scattering, Chapter 13. In *Comprehensive Guide for Mesoporous Materials, Volume 1: Synthesis and Characterization*; Aliofkhazraei, M., Ed.; Nova Science Publishers: New York, NY, USA, 2015; Volume 1.
43. Fernandes, F.R.D.; Pinto, F.G.H.S.; Lima, E.L.F.; Souza, L.D.; Caldeira, V.P.S.; Santos, A.G.D. Influence of Synthesis Parameters in Obtaining KIT-6 Mesoporous Material. *Appl. Sci.* **2018**, *8*, 725. [CrossRef]
44. Taghizadeh, M.; Akhoundzadeh, H.; Rezayan, A.; Sadeghian, M. Excellent catalytic performance of 3D-mesoporous KIT-6 supported Cu and Ce nanoparticles in methanol steam reforming. *Int. J. Hydrogen Energy* **2018**, *43*, 10926–10937. [CrossRef]
45. Broyer, M.; Valange, S.; Bellat, J.P.; Bertrand, O.; Weber, G.; Gabelica, Z. Influence of Aging, Thermal, Hydrothermal, and Mechanical Treatments on the Porosity of MCM-41 Mesoporous Silica. *Langmuir* **2002**, *18*, 5083–5091. [CrossRef]
46. Su, Y.; Dai, L.; Zhang, Q.; Li, Y.; Peng, J.; Wu, R.; Han, W.; Tang, Z.; Wang, Y. Fabrication of Cu-Doped CeO_2 Catalysts with Different Dimension Pore Structures for CO Catalytic Oxidation. *Catal. Surv. Asia* **2016**, *20*, 231–240. [CrossRef]
47. Wang, Y.; Oord, R.; Berg, D.v.D.; Weckhuysen, B.M.; Makkee, M. Oxygen vacancies in reduced Rh/ and Pt/ceria for highly selective and reactive reduction of NO into N_2 in excess of O_2. *ChemCatChem* **2017**, *9*, 2935–2938. [CrossRef]
48. Thommes, M.; Kaneko, K.; Neimark, A.V.; Olivier, J.P.; Rodriguez-Reinoso, F.; Rouquerol, J.; Sing, K.S.W. Physisorption of gases, with special reference to the evaluation of surface area and pore size distribution (IUPAC technical report). *Pure Appl. Chem.* **2015**, *87*, 1051–1069. [CrossRef]
49. Kishor, R.; Ghoshal, A.K. Understanding the hydrothermal, thermal, mechanical and hydrolytic stability of mesoporous KIT-6: A comprehensive study. *Microporous Mesoporous Mater.* **2017**, *242*, 127–135. [CrossRef]
50. Florek, J.; Guillet-Nicolas, R.; Kleitz, F. Ordered mesoporous silica: Synthesis and applications, Chapter 4. In *Functional Materials*; Leclerc, M., Gauvin, R., Eds.; De Gruyter: Berlin, Germany, 2014.
51. Gao, C.; Zhang, Q.; Lu, Z.; Yin, Y. Templated synthesis of metal nanorods in silica nanotubes. *J. Am. Chem. Soc.* **2011**, *133*, 19706–19709. [CrossRef]
52. Deng, X.; Chen, K.; Tüysüz, H. Protocol for the nanocasting method: Preparation of ordered mesoporous metal oxides. *Chem. Mater.* **2017**, *29*, 40–52. [CrossRef]
53. Pan, C.; Zhang, D.; Shi, L. CTAB assisted hydrothermal synthesis, controlled conversion and CO oxidation properties of CeO_2 nanoplates, nanotubes, and nanorods. *Cryst. Growth Des.* **2008**, *181*, 1298–1306. [CrossRef]
54. Shannon, R.D. Revised effective ionic radii and systematic studies of interatomic distances in halides and chalcogenides. *Acta Cryst.* **1976**, *A32*, 751–767. [CrossRef]
55. Abu Bakar, M.Z.; Juhari, J.; Abdullah, A.Z. Effect of hydrothermal treatment aging temperature of silica template on the formation of mesoporous SnO_2 materials. In Proceedings of the IOP Conference Series: Earth and Environmental Science, Kuala Lumpur, Malaysia, 21–22 October 2025; Volume 1516, p. 012009. [CrossRef]
56. Juhari, J.; Abu Bakar, M.Z.; Abdullah, A.Z. Nanocasting route for the synthesis of ordered mesoporous SnO_2 with highly crystalline framework. *J. Mater. Sci. Eng. B* **2014**, *4*, 203–209. [CrossRef]
57. Mi, R.; Li, D.; Hu, Z.; Yang, R.T. Morphology effects of CeO_2 nanomaterials on the catalytic combustion of toluene: A combined kinetics and diffuse reflectance infrared Fourier transform spectroscopy study. *ACS Catal.* **2021**, *11*, 7876−7889. [CrossRef]

58. Pahi, S.; Sahu, S.; Singh, S.K.; Behera, A.; Patel, R.K. Visible light active Zr- and N-doped TiO_2 coupled g-C_3N_4 heterojunction nanosheets as a photocatalyst for the degradation of bromoxynil and Rh B along with the H_2 evolution process. *Nanoscale Adv.* **2021**, *3*, 6468. [CrossRef] [PubMed]
59. Bazhukova, I.N.; Sokovnin, S.Y.; Ilves, V.G.; Myshkina, A.V.; Vazirov, R.A.; Pizurova, N.; Kasyanova, V.V. Luminescence and optical properties of cerium oxide nanoparticles. *Opt. Mater.* **2019**, *92*, 136–142. [CrossRef]
60. Phoka, S.; Laokul, P.; Swatsitang, E.; Promarak, V.; Seraphin, S.; Maensiri, S. Synthesis, structural and optical properties of CeO_2 nanoparticles synthesized by a simple polyvinyl pyrrolidone (PVP) solution route. *Mater. Chem. Phys.* **2009**, *115*, 423–428. [CrossRef]
61. Zafar, M.; Mahmood, S.; Shaikh, H.; Alhamidi, A.; Ramay, S.M.; Saleem, M.; A Siddiqi, S. Structural, dielectric and optical investigations of Zr incorporated ceria nanoparticles. *Mater. Res. Express* **2019**, *6*, 116321. [CrossRef]
62. Parveen, T.; Ahmad, I.; Aslam, M.; Fozia, F.; Khushal, A.; Mohany, M.; Al-Rejaie, S.S.; Ziaullah, Z.; Milošević, M. Green synthesis of pure and zirconium-doped cerium oxide nanoparticles using aqueous extract of *Sanvitalia procumbens*, its characterization, antiplatelet and cytotoxic activities. *Nanomater. Nanotechnol.* **2025**, *2025*, 4276075. [CrossRef]
63. Tsunekawa, S.; Wang, J.-T.; Kawazoe, Y.; Kasuya, A. Blueshifts in the ultraviolet absorption spectra of cerium oxide nanocrystallites. *J. Appl. Phys.* **2003**, *94*, 3654–3656. [CrossRef]
64. Sahoo, S.K.; Mohapatra, M.; Anand, S. Absorption and emission properties of Zr-doped nanoceria synthesised by co-precipitation-hydrothermal treatment route. *J. Exp. Nanosci.* **2015**, *10*, 1012–1027. [CrossRef]
65. Arul, N.S.; Mangalaraj, D.; Chen, P.C.; Ponpandian, N.; Viswanathan, C. Viswanathan, String quantum confinement effect in nanocrystalline cerium oxide. *Mater. Lett.* **2011**, *65*, 2635–2638. [CrossRef]
66. Kuchibhatla, S.V.; Karakoti, A.S.; Baer, D.R.; Samudrala, S.; Engelhard, M.H.; Amonette, J.E.; Thevuthasan, S.; Seal, S. Influence of Aging and Environment on Nanoparticle Chemistry—Implication to Confinement Effects in Nanoceria. *J. Phys. Chem. C* **2012**, *116*, 14108–14114. [CrossRef] [PubMed]
67. Filtschew, A.; Hofmann, K.; Hess, C. Ceria and its defect structure: New insights from a combined spectroscopy approach. *J. Phys. Chem. C* **2016**, *120*, 6694–6703. [CrossRef]
68. Zhang, F.; Chen, C.; Hanson, J.C.; Robinson, R.D.; Herman, I.P.; Chan, S.-W. Phases in ceria-zirconia binary oxide (1-x)CeO_2-xZrO_2 nanoparticles, the effect of particle size. *J. Am. Ceram. Soc.* **2006**, *89*, 1028–1036. [CrossRef]
69. Loridant, S. Raman spectroscopy as a powerful tool to characterize ceria-based catalyst. *Catal. Today* **2021**, *373*, 98–111. [CrossRef]
70. Kainbayev, N.; Sriubas, M.; Virbukas, D.; Rutkuniene, Z.; Bockute, K.; Bolegenova, S.; Laukaitis, G. Raman study of nanocrystalline-doped ceria oxide tin film. *Coatings* **2020**, *10*, 432. [CrossRef]
71. Scavini, M.; Bertolotti, F.; Mlloja, J.; Umbri, F.; Bosc, A.; Cappelli, S.; Checchia, S.; Oliva, C.; Fumagalli, P.; Ceresoli, D.; et al. Structure and surface relaxation of CeO_2 nanoparticles unveiled by combining real and reciprocal space total scattering analysis. *Nanomaterials* **2022**, *12*, 3385. [CrossRef]
72. Li, L.; Li, P.; Wang, Y.; Lin, L.; Shah, A.H.; He, T. Modulation of oxygen vacancy in hydranges-like ceria via Zr doping for CO_2 photoreduction. *Appl. Surf. Sci.* **2018**, *452*, 498–506. [CrossRef]
73. Deus, R.C.; Amoresi, R.A.C.; Desimone, P.M.; Schipani, F.; Rocha, L.S.R.; Ponce, M.A.; Simoes, A.Z.; Longo, E. Electrical behavior of cerium dioxide films exposed to different gasses atmospheres. *Ceram. Int.* **2016**, *42*, 15023–15029. [CrossRef]
74. Liao, Y.; Fu, M.; Chen, L.; Wu, J.; Huang, B.; Ye, D. Catalytic oxidation of toluene over nanorod-structured Mn−Ce mixed oxides. *Catal. Today* **2013**, *216*, 220–228. [CrossRef]
75. Tulebekov, Y.; Orazov, Z.; Satybaldiyev, B.; Snow, D.D.; Schneider, R.; Uralbekov, B. Reaction steps in heterogeneous photocatalytic oxidation of toluene in gas phase—A review. *Molecules* **2023**, *28*, 6451. [CrossRef]
76. Tomašić, V.; Jović, F.; Gomzi, Z. Photocatalytic oxidation of toluene in the gas phase: Modelling an annular photocatalytic reactor. *Catal. Today* **2008**, *137*, 350–356. [CrossRef]

https://doi.org/10.3390/cryst16020083